Scripta Materialia 260 (2025) 116598

Contents lists available at ScienceDirect

Scripta Materialia

journal homepage: www.journals.elsevier.com/scripta-materialia

Architected superalloys: A pathway to lightweight high temperature materials

Yuanbo T. Tang [a,b,*], Yunlan Zhang [c], Li Wan [c], Nicole Kuek [d], Enrique Alabort [d], Roger C. Reed [a,b]

[a] School of Metallurgy and Materials, University of Birmingham, Elms Road, Birmingham, B15 2SE, United Kingdom
[b] Department of Materials, University of Oxford, Parks Road, Oxford, OX1 3PH, United Kingdom
[c] Department of Civil, Architectural and Environmental Engineering, The University of Texas at Austin, 301E. Dean Keeton St., Stop C1792, Austin, TX 78712, USA
[d] Alloyed Ltd., Unit 15, Oxford Industrial Park, Yarnton OX5 1QU, United Kingdom

ARTICLE INFO

Keywords:
Superalloy
Lattice
Honeycomb
Architected material
High temperature
Deformation

ABSTRACT

Materials for high temperature applications – for example rocket engines – are often metallic and therefore tend to suffer from high density when used in their monolithic form. The root cause of this dilemma is the solid-state physics causing the low rates of thermally-activated processes such as diffusion and creep, it also confers the very high density. Using the nickel-based superalloys as an exemplar, we demonstrate here that this dilemma in high temperature materials can be defeated by designing open cellular structures – leveraging recent progress in new alloys designed specifically for additive manufacturing. The resulting low-density architected materials exhibit optimal stretch-dominant or bend-dominant behaviour at high temperatures, as exemplified by regular honeycomb structures which are built. Thus, as well-behaved materials these findings open up new design possibilities for high-temperature applications where low density is particularly needed.

Metals and alloys are required to operate at elevated temperatures, for example in critical sectors including aeronautics, space, automotive and energy generation – underscoring their versatility and essential roles in modern technologies [1]. Examples include combustors for rocket engines, topology-optimised structures for launch vehicles, the fabrication of thermal shields for spacecraft re-entry, sophisticated turbomachinery, and the development of powertrains for high-performance vehicles. But what properties inform the best choice for such applications? The answer lies in a capacity to resist thermally-activated processes such as diffusion, creep deformation, oxidation which – if not designed against by optimised choice of metal solvent, alloying elements, and microstructural engineering of precipitate structures – leads to excessive rates of degradation and hence structural failure. The nickel-based superalloys are exemplars, distinguished by their extraordinary high temperature strength and toughness, resilience to creep-fatigue, microstructural stability and resistance to corrosion [2,3]. Nevertheless, it is an unfortunate fact that the very same solid-state physics which confers low rates of thermally-activated processes – for example the configuration of the d-shell electrons in the transition metals – endows alloys which tend to be dense [4]. Thus for example nickel has a relative density of 8.9 and in the superalloys, the necessary alloying by refractory elements such as W, Re and Ta (relative densities are 20, 21 and 17 respectively) exacerbates this. This represents their Achilles' heel. Circumventing this density dilemma is a major unsolved challenge in this field.

How best to deal with this impasse? The strategy adopted here is to make use of the revolution in design possibilities unfolding from the advancement of metal additive manufacturing – especially the emerging group of hollow, architected materials which can be designed to be ultra-stiff, lightweight and even capable of responding to external stimuli through tailoring geometry and topology [5,6]. Thus in this way traditional monolithic, heavy components are avoided and replaced by multifunctional hollow structures of greater geometrical complexity [7]. Nevertheless, for the high temperature materials such as the superalloys these can be exceptionally hard to manufacture due to a vulnerable solidification path – enriched solutes in the last liquid that lead to solidification cracks and strain-age cracking due to the development of precipitation after reheating [8]. Typical microstructural defects such as extensive microcracking that arise from the manufacturing process are shown in Fig. 1 (a-c). Fortunately, recent materials breakthroughs

* Corresponding author.
E-mail address: y.t.tang@bham.ac.uk (Y.T. Tang).

https://doi.org/10.1016/j.scriptamat.2025.116598
Received 8 December 2024; Received in revised form 27 January 2025; Accepted 4 February 2025
Available online 10 February 2025

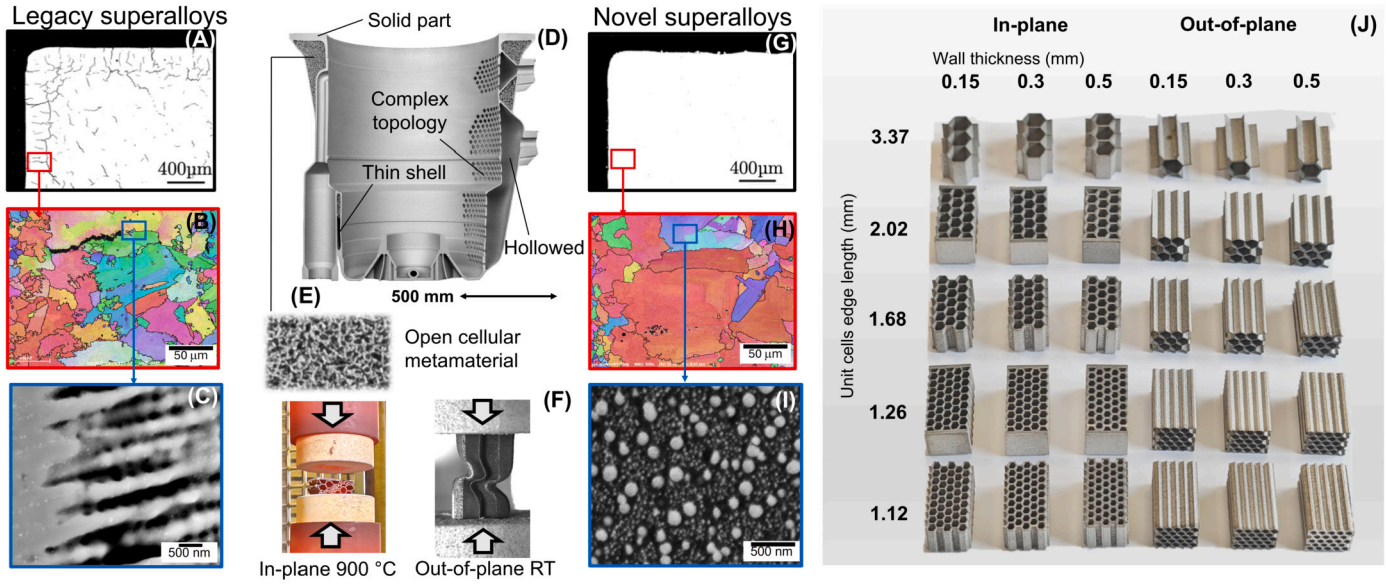

Fig. 1. Overview of conceptual parts utilising open-cellular metamaterials manufactured by Alloyed Ltd and typical 3D printed superalloy microstructures and defects are shown in three length scales for legacy and novel superalloys. (a-c) shows binarised optical micrograph, inverse pole figure of grain structures near an intergranular crack and secondary electron image of a solidification crack for a typical non-printable legacy superalloy [9]. (d) illustrates a manufactured aerospace demonstrator utilising topological design for lightweighting, where (e) highlights the open-cellular metamaterials used. (f) shows uniaxial compression testing at 900 °C and room temperature captured by video extensometer. (g-i) shows binarised optical micrograph, inverse pole figure of grain structures and secondary electron image of the strengthening precipitates for the novel printable superalloy studied here [9]. The tested honeycomb geometries are shown in (j).

have arisen in additive manufacturing – involving advanced, printable superalloys that maintain integrity at high temperatures, see Fig. 1 (g-i) – which allow defect-free, precipitation-strengthened microstructures conferring the performance required [9,10].

Nevertheless, the possible deployment of these materials at elevated temperatures raises critical questions about their behaviour – particularly due to the damage mechanisms which are likely to be very different from the monolithic case. The resilience of high-temperature architected materials against these challenges remains unexplored, posing crucial concerns about their long-term reliability and potential for unprecedented behaviour under such demanding conditions. This work focuses on demonstrating the necessary processing and highlights the fundamental research issues concerning mesoscale mechanics during deformation linking to the various damage routes. To date, this area has been under explored, making the design of high-temperature lattice structures unrealistic for mission-critical applications. In what follows, we focus on idealised honeycomb structures to uncover the underlying damage and failure mechanisms, deliberately avoiding the complexities of more intricate geometries that could complicate interpretation. These honeycombs are subjected to deformation in both in-plane and out-of-plane directions, enabling the exploration of ideal bend- and stretch-dominant behaviours. We selected the ABD-900AM superalloy for its exceptional printability and high-temperature performance [11], testing it at both room temperature and 900 °C across a range of relative densities spanning approximately one decade. Different deformation modes are studied as a function of temperature and t/l ratio (cell wall thickness/length). The results are rationalised by a meso-mechanics modelling using finite element analysis (FEA) incorporating appropriate damage criteria. The experimental results and accuracy of our computations confirm the extension of the design space for these materials. Our results confirm the arrival of high temperature materials of exceptionally low density and great geometrical precision.

Honeycomb structures in this study have the unit cells designed in-plane (x-y) and out-of-plane (x-z), see Fig. 1 (j). The geometry of each structure was confined within the dimensions of $10 \times 17.5 \times 10$ mm^3 (xyz). The honeycomb structures were all regular hexagons, with different unit cell sizes and wall thicknesses, which gives the t/l ratio (or relative density) ranging between 0.05 to 0.45. A breakdown of the geometry design for each structure is shown in Table 1 in the appendix. Manufacturing of the hollow specimens were conducted using laser-powder bed fusion (L-PBF) with Renishaw 400 machine, where technical specification and composition were given in [12]. The build direction is parallel to the z-axis of the honeycombs in all cases. All samples were tested in the as-printed state.

Mechanical properties of the honeycomb lattices were evaluated using an Instron 8852 machine at room temperature and at 900 °C. Compressive load was applied along the long direction (y-axis) via compression grips with two SiC platens. Strain was measured using an Imetrum video extensometry system by tracking speckled patterns. High temperature tests were conducted using a bespoke split furnace (Severn Thermal Solutions, UK) with a heating rate of 20-30 °C/min, monitored using two type-K thermocouples in contact with the push rods. A holding temperature of 10 mins and a strain rate of 5×10^{-3} s^{-1} were employed. In order to assist modelling, conventional tensile tests at both temperatures and strain rates were carried out with the same material in solid (bulk) form. The solid specimens were additively manufactured using the same laser parameters into a cylindrical geometry with a gauge diameter of 3.5 mm and gauge length of 6 mm. They were tested in the as-printed state. Scanning electron microscopy (SEM) were used to study the microstructures before and after deformation. A Zeiss Merlin SEM was operated at 15 kV acceleration voltage. Secondary and backscattered electron detectors were used. A BRUKER electron backscattered diffraction (EBSD) HR-flash detector and an Oxford Instrument X-MAX energy dispersive x-ray spectroscopy (EDS) were used to probe crystallographic and compositional information.

Numerical simulations were performed using the commercial software ABAQUS (Explicit, 2023). To study the in-plane behaviour of honeycomb structures, models were developed to replicate the experimental specimens, employing 4-node bilinear plane stress elements for mesh discretisation. To capture the out-of-plane behaviour, 4-node doubly curved thin and thick shell element are used for analysis. A detailed convergence study determined that an optimal mesh size of one-quarter of the specimen thickness (t/4) is sufficient to accurately capture the in-plane behaviour while maintaining computational efficiency (Fig. S1 A). For out-of-plane behaviour, the analysis revealed that an element size of one-eighth of the specimen length (L/8) is necessary to achieve

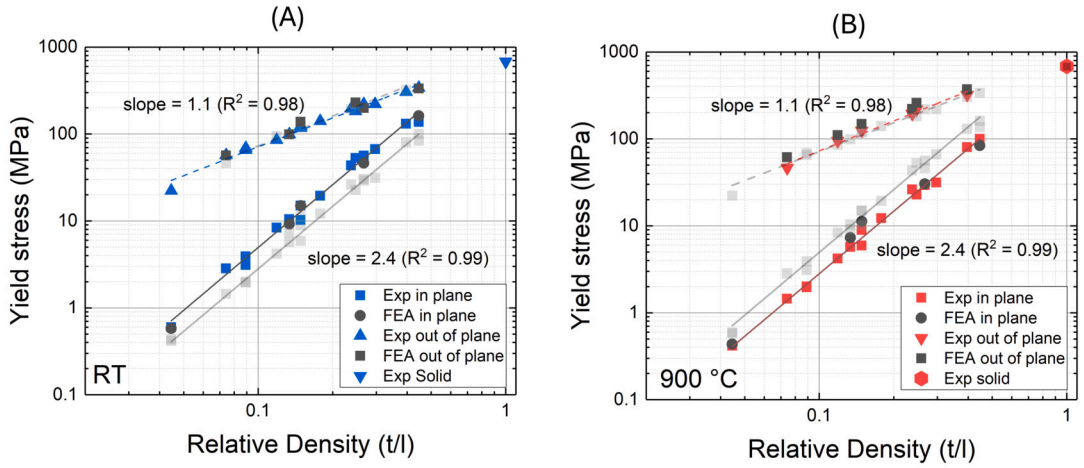

Fig. 2. Yield strength and relative density plot in log-log scale for in-plane and out-of-plane honeycomb by uniaxial compression by experiment and FEA simulation at room temperature (a) and 900 °C (b).

reliable results (Fig. S1 B). Both element sizes were employed in the analysis to ensure comprehensive coverage of in-plane and out-of-plane responses. To minimise hourglass effects and dynamic effects, a loading rate of 6.25 mm/s was carefully selected. The validity of this rate was confirmed by maintaining the ratios of artificial energy to internal energy below 5% (Fig. S2).

We first tested the overall compression mechanics of the honeycomb structures – in both out-of-plane and in-plane loading directions at room temperature and 900 °C. Various samples were characterised by altering the aspect ratio of each honeycomb cell wall – the thickness-to-length (t/l) ratio – which influences directly the relative density in regular honeycombs. The strength of all specimens obtained from experiments and simulations are presented in the form of log-log plots (Fig. 2). The room temperature results are shown in colour in Fig. 2 (a) with the high temperature data in grey transparent, and vice-versa for high temperature in Fig. 2 (b). The specimens displayed both brittle and ductile behaviour, influenced by temperature and geometry. For ductile failures, yield strength was determined at 0.2% engineering strain, whereas for brittle failures, peak stress was used. The 0.2% yield strength of solid material is also plotted in both graphs as a benchmark.

By extracting the slope from yield strength and relative density in each testing orientation as in Fig. 2, we found linear relationships for out-of-plane and in-plane behaviour, with extrapolation to the solid material's yield strength regardless of the effect of temperature. The slope (n) describing the mode of deformation is as proposed by Gibson & Ashby [13], with $n = 1$ suggesting that the materials exhibit ideal stretching behaviour (out-of-plane), while the slope $n = 2$ indicates ideal bending behaviour (in-plane). At room temperature, the best-fit slope is $n = 2.4$ for in-plane deformation and $n = 1.1$ for out-of-plane deformation. The slight discrepancy of our results with the analytical values may possibly arise from edge effects and hence may be affected by unconstrained boundaries that can deform freely.

High-temperature deformation was found to differ significantly from room temperature behaviour – here the Gibson-Ashby relationship is verified for the first time. Both in-plane and out-of-plane deformation exhibit consistent slope values in each orientation: $n = 2.4$ and $n = 1.1$, respectively, see Fig. 2 (b). While the slope for in-plane deformation remains consistent across different temperatures, it shifts downward, indicating a 43% reduction in strength at a given density as compared to room temperature. In contrast, out-of-plane deformation remains unchanged, with overlapping slopes at both temperatures. This observation is indicative of a shift in the local failure mechanism from in-plane to out-of-plane under high-temperature conditions.

In order to glean further insights into the deformation characteristics, the full stress-strain behaviour was analysed. A representative honeycomb sample with a cell edge length of 2.02 mm, thickness of 0.3 mm, and a relative density (or (t/l)) of 0.15 was considered in detail. The compression stress-strain behaviour is illustrated in Fig. 3 (a-d) via both experimental data and finite element analysis (FEA) simulations. At room temperature, the in-plane deformation exhibits a classical plateau following the yield point, with moderate progressive hardening as additional cell walls fold contributing to densification. The stress-strain characteristics are closely mirrored by the FEA simulation results, with the yield point, hardening, and folding strain aligning well with the experimental observations. However, the deformation behaviour at 900 °C, shown in Fig. 3 (b), differs notably. The in-plane honeycomb specimen undergoes brittle collapse after the initial elastic peak, with no plastic behaviour evident and a catastrophic load drop occurring at just 1.7% elongation. In contrast, for out-of-plane behaviour, the material shows varying levels of work hardening at room temperature depending on thickness. At 900 °C, while no significant work hardening is observed, a gradual failure occurs, as opposed to the catastrophic fracture seen in the in-plane case.

The in-plane honeycomb at 900 °C reveals a macroscopic brittle fracture, whereas the solid material exhibits a reasonable elongation to failure of 8% under the same testing conditions. This is a pronounced asymmetrical mechanical response of the cellular and solid superalloy, which is intriguing. In addition to this, neither the room temperature deformation nor the out-of-plane deformation at 900 °C showed signs of brittle collapse. Visual examination confirms that the fractured specimens shattered into pieces, with fractures consistently originating at the vertices (junctions), while the cell walls remained intact with no clear signs of bending. This embrittlement behaviour in the high-temperature honeycomb is likely rooted in the material's intrinsic resistance to plastic instability, a characteristic determined by its work hardening coefficient. As shown in Fig. 3 (f), during work hardening, further loading strengthens the cross-sections that have undergone deformation, thereby redistributing the load. At room temperature, work hardening diminishes at around 30% true strain, indicating sufficient tolerance for damage nucleation. In contrast, at 900 °C, the material work-softens, tolerating only about 2% true strain – beyond this point, localised damage emerges, leading to a loss of load-bearing capacity. There is a particular vulnerability to in-plane deformation because bending at hinges exacerbates deflection and increases local strain. As a result, it is confirmed that stretch-dominant structures – such as these out-of-plane honeycombs – do not experience the same reduction in strength as their room temperature counterparts.

The role of microstructural features is examined as follows. We first analyse in-plane honeycombs deformed at room temperature with varying t/l ratios, as shown in Fig. 4 (a) and (c). These conditions under comparison have the same cell length (2.02 mm) but different wall thicknesses of 0.15 mm and 0.5 mm, resulting in t/l ratios of 0.074 and 0.25, respectively. The low t/l sample shows complete folding of cell

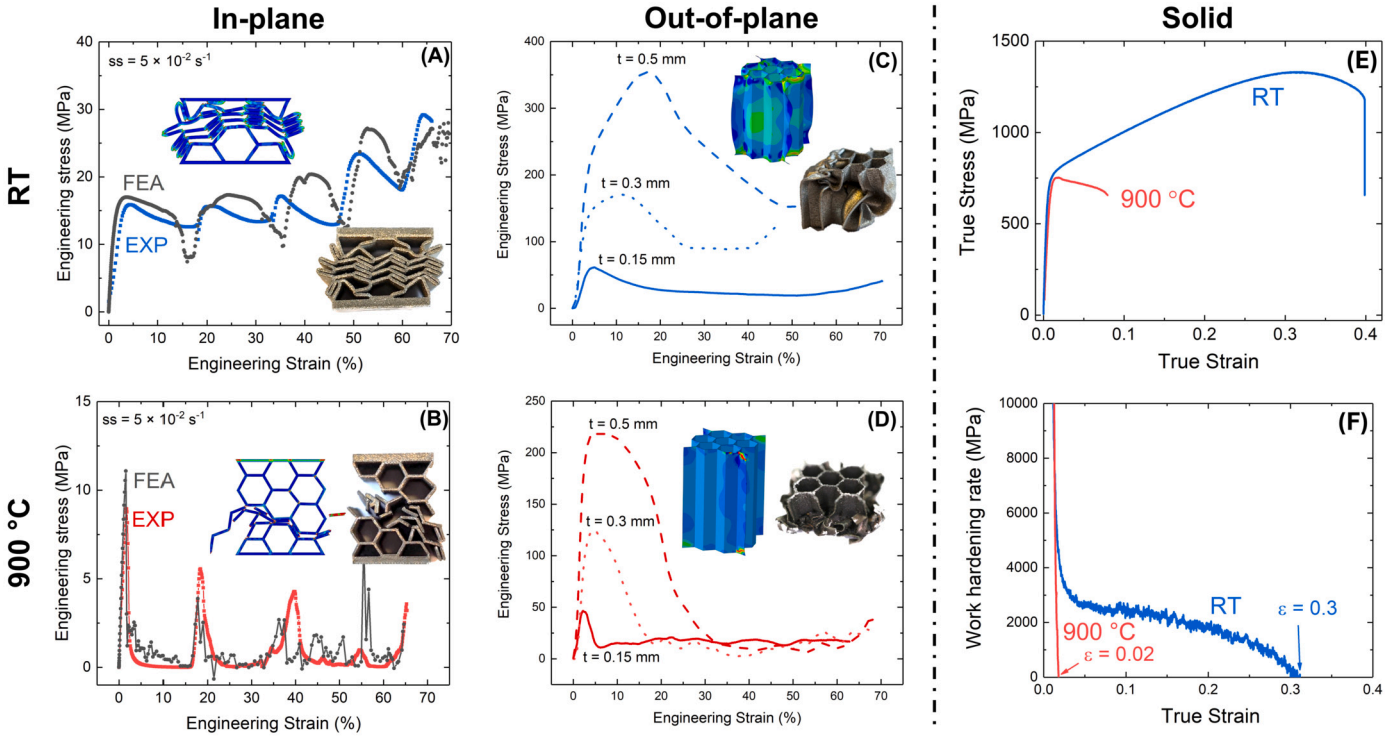

Fig. 3. Engineering compression stress strain curves for a typical honeycomb sample by experiment and FEA simulation. (a) and (b) show in-plane deformation in room temperature and 900 °C. (c) and (d) show out-of-plane deformation in room temperature and 900 °C by experiment. (e) illustrates the true stress strain curve of the solid material ABD-900AM in room temperature and 900 °C measured with typical dog bone samples and (f) shows the corresponding work hardening rate evolution. All mechanical tests were carried out at a strain rate of 5×10^{-3} s^{-1}.

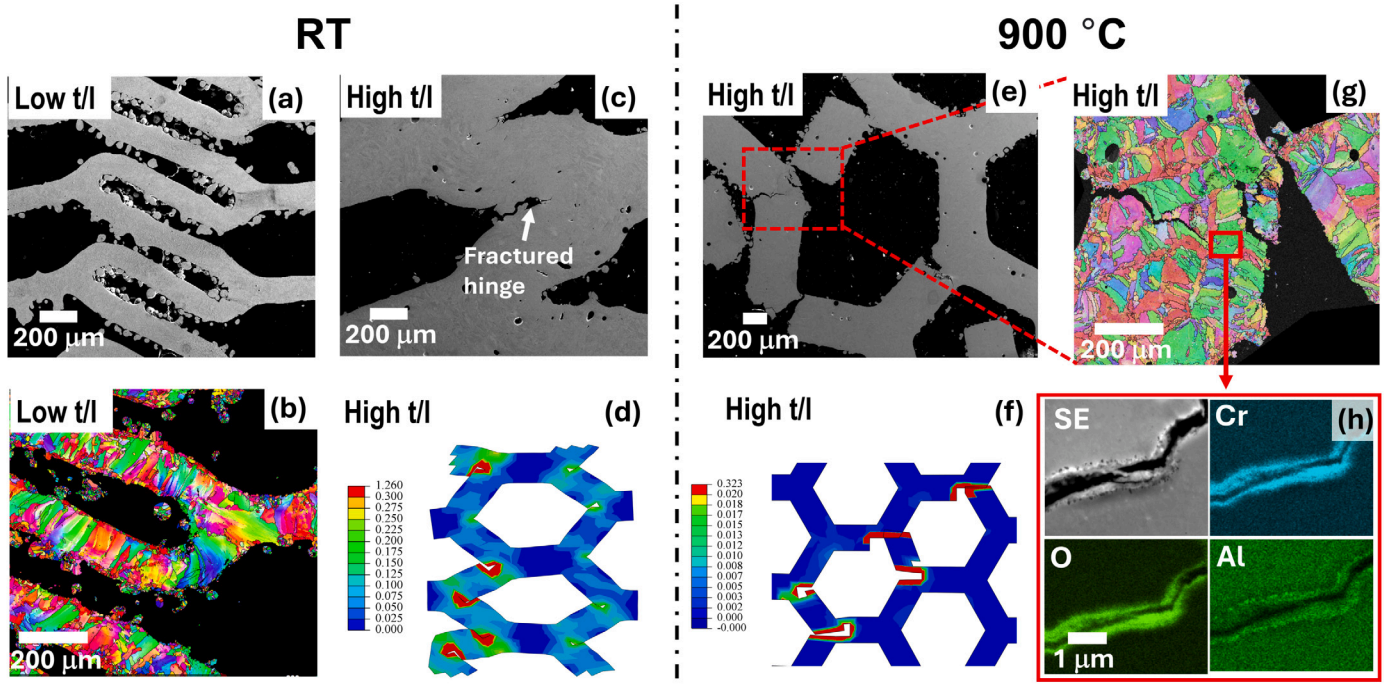

Fig. 4. Microstructure and simulation of in-plane deformed honeycomb structure. (a) and (b) secondary electron image and IPF map of a low t/l honeycomb deformed at room temperature. (c) and (d) show the secondary electron image and FEA simulation for a high t/l specimen deformed at room temperature, where short cracks can be observed. (c) and (d) highlight crack propagation across the structure in secondary electron image and FEA simulation for a high t/l specimen deformed at 900 °C. (g) illustrates the grain structures at a vertex revealing grain boundary cracks. (h) demonstrates the oxidation scale thickness by chemical mapping.

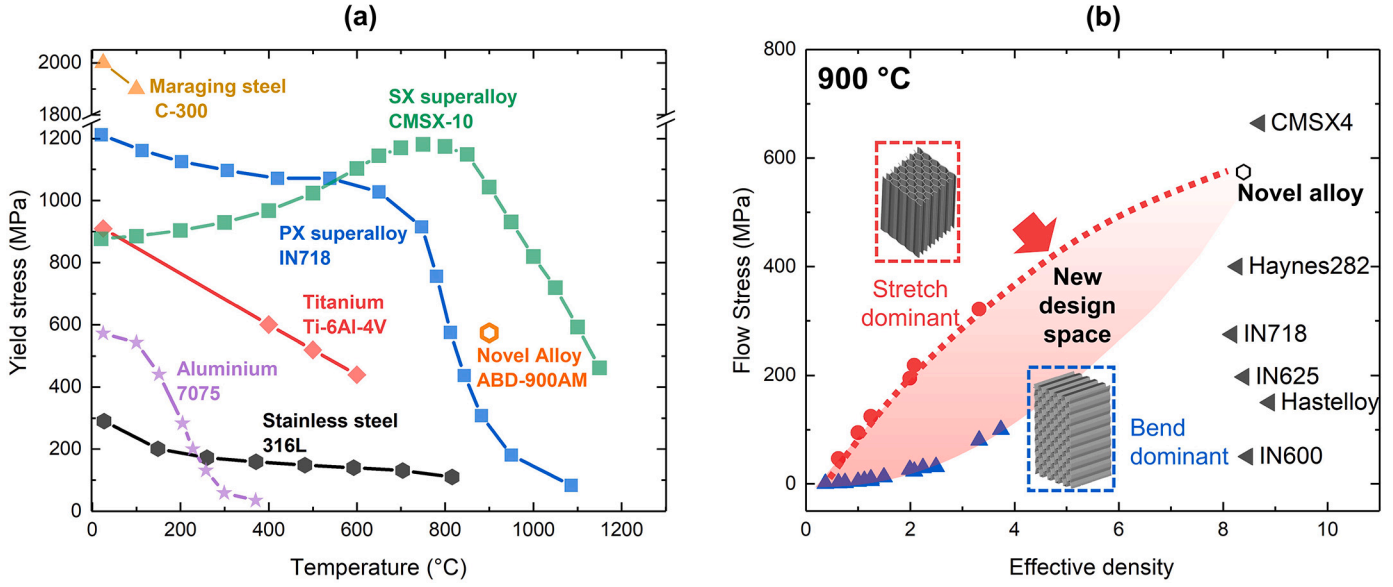

Fig. 5. Yield strength of major classes of commercial structural alloys as a function of temperature is shown in (a). High temperature strength at 900 °C vs density of commercial alloys with honeycomb structures in this work shown in (b). The new design space discovered is shaded in light red. (For interpretation of the colours in the figure(s), the reader is referred to the web version of this article.)

walls without any microstructural damage, whereas the high t/l sample reveals short cracks at some vertices, extending up to approximately ~200 μm, as depicted in Fig. 4 (c). The FEA results in (d) accurately replicate these damage events at the same locations and also show significant plastic deformation in the cell walls. The damage observed in the high t/l sample suggests that intrinsic ductility alone cannot fully prevent internal damage as relative density increases. As the member aspect ratio increases, the deformation mode shifts from hinging to shearing.

For the same honeycomb deformed at high temperature, long cracks through wall thicknesses are frequently observed at vertices. Electron backscattered diffraction (EBSD) reveals that the cracks only occur at the high angle grain boundaries, which often is the weak microstructural link at elevated temperatures [14]. These cracks nucleate from one vertex and quickly propagate through the entire cross-section of the macrostructure in form of shear bands; thus the sample loses load-bearing capacity rapidly when the first damage occurs. The formation of such shear bands is demonstrated in Fig. 4 (f). In contrast to the room temperature deformation (d), load redistribution no longer occurs instead strain localisation becomes the operative mechanism. Further chemical analysis was carried out at the crack tips to probe the role of oxidation in Fig. 4 (h), where some thin chromia and alumina scales were observed. However, their thickness remained on the scale of ~200 nm, hence they are unlikely to be pivotal in promoting cracks propagation.

One must consider the ramifications of these findings. It is useful to consider the yield strength of the major alloy systems see Fig. 5 (a) across a wide temperature range. Six classes of metallic materials with their flagship examples are plotted up to their working temperature range, where data were taken from the literature. The alloys selected are stainless steel (SS316) [15], ultra high-strength maraging steels (C-300) [16], high strength aluminium (7075) [17], titanium (Ti-6Al-4V) [18], polycrystalline nickel superalloy (IN718) [19] and single crystal nickel superalloy (CMSX-10) [4]. The yield strength of each alloy generally decreases with increasing temperature, with the exception of the single crystal superalloy showing an increase up to around 750 °C before decreasing, consistent with the so-called 'anomalous yielding' behaviour. Light alloys, such as aluminium and titanium, typically have low heat resistance, with maximum working temperatures around 250 °C and 600 °C, respectively. Aluminium is limited by its melting point of 660 °C, while titanium becomes excessively reactive and loses thermal stability at higher temperatures [20]. Maraging steels also suffer from adverse thermal decomposition, making them unreliable at elevated temperatures. Stainless steels, particularly those with an austenitic crystal structure, maintain structural integrity up to approximately 800 °C, though their strength is significantly lower than that of superalloys, making them suitable only for non-critical load-bearing applications. Beyond 600 °C, the high-temperature regime is dominated by superalloys, which are designed to retain their mechanical properties under extreme conditions.

To illustrate the compelling case for these new lightweight high-temperature materials, we present in Fig. 5 (b) the performance of in-plane and out-of-plane honeycombs made from ABD-900AM at 900 °C as a function of density. For comparison, the typical strength of nickel-based superalloys – which have densities ranging between 8-9 g/cm^3 – is also plotted. This study demonstrates clearly that the honeycomb structures occupy a brand-new design space, characterised by a remarkably low effective density, down to 0.43 g/cm^3. Additionally, their structural and mechanical properties are fully tunable by adjusting the internal architecture, highlighting the potential for high-temperature structural applications with exceptionally low densities.

To summarise, for the future design of high-temperature architected materials, three key insights have emerged from this work. First, the creation of cellular structures in order to reduce the effective density of high temperature materials is viable. The nickel-based superalloys are good candidates for this. This cannot be done with aluminium, magnesium, or titanium due to their inherent physical limitations such as low melting points and/or poor oxidation resistance. Second, stretch-dominant structures are less sensitive to local damage evolution, making them appealing for applications requiring ultra-high specific strength. Third, bend-dominant structures carry a generic risk of brittle collapse to cause irreparable damage at low macroscopic strain and compromising energy absorption capabilities. This is driven by local damage evolution rather than load redistribution – which is further exacerbated by strain softening, which is an unavoidable issue at high temperatures. But enhancing creep resistance and intrinsic grain boundary strength might well help to mitigate this risk.

It is demonstrated that superalloy-based cellular structures can be designed and fabricated with a wide range of relative densities and mechanical properties, opening up a new design space for materials usage at elevated temperatures – so far yet to be achieved with other low-density materials. Thus it is confirmed that advances in additive manufacturing (AM) processing and materials development enable the

creation of multifunctional architected materials with unprecedented performance. Here, we have concentrated upon regular honeycombs but future research should focus on designing and evaluating even more complex structures.

CRediT authorship contribution statement

Yuanbo T. Tang: Writing – review & editing, Writing – original draft, Supervision, Investigation, Formal analysis, Data curation, Conceptualization. **Yunlan Zhang:** Writing – review & editing, Methodology, Investigation, Formal analysis, Data curation. **Li Wan:** Investigation, Formal analysis, Data curation. **Nicole Kuek:** Methodology, Investigation. **Enrique Alabort:** Methodology, Investigation, Conceptualization. **Roger C. Reed:** Writing – review & editing, Investigation, Formal analysis.

Declaration of competing interest

The authors declare that they have no known competing financial interests or personal relationships that could have appeared to influence the work reported in this paper.

Acknowledgements

The authors are grateful for Alloyed Ltd for provision of materials used in this study.

Appendix

Table 1
Appendix: Geometry design of the honeycomb specimens tested.

Sample number	# unit cell along y-axis (17.5 mm)	Unit cell size (mm)	wall thickness (mm)	t/l ratio	measured relative density
1	3	5.83	0.15	0.05	0.05
2	3	5.83	0.3	0.09	0.09
3	3	5.83	0.5	0.15	0.15
4	5	3.50	0.15	0.07	0.09
5	5	3.50	0.3	0.15	0.17
6	5	3.50	0.5	0.25	0.26
7	6	2.92	0.15	0.09	0.10
8	6	2.92	0.3	0.18	0.19
9	6	2.92	0.5	0.30	0.29
10	8	2.19	0.15	0.12	0.13
11	8	2.19	0.3	0.24	0.25
12	8	2.19	0.5	0.40	0.40
13	9	1.94	0.15	0.13	0.14
14	9	1.94	0.3	0.27	0.26
15	9	1.94	0.5	0.45	0.43

Appendix. Supplementary material

Supplementary material related to this article can be found online at https://doi.org/10.1016/j.scriptamat.2025.116598.

References

[1] T.M. Pollock, Alloy design for aircraft engines, Nat. Mater. 15 (2016) 809–815.
[2] C. Panwisawas, Y.T. Tang, R.C. Reed, Metal 3D printing as a disruptive technology for superalloys, Nat. Commun. 11 (2327) (2020).
[3] A. Mostafaei, R. Ghiaasiaan, I.-T. Ho, S. Strayer, K.-C. Chang, N. Shamsaei, S. Shao, S. Paul, A.-C. Yeh, S. Tin, A.C. To, Additive manufacturing of nickel-based superalloys: a state-of-the-art review on process-structure-defect-property relationship, Prog. Mater. Sci. 136 (2023) 101108.
[4] R.C. Reed, The Superalloys: Fundamentals and Applications, Cambridge University Press, 2006.
[5] M. Benedetti, A. du Plessis, R. Ritchie, M. Dallago, N. Razavi, F. Berto, Architected cellular materials: a review on their mechanical properties towards fatigue-tolerant design and fabrication, Mater. Sci. Eng., R Rep. 144 (2021) 100606.
[6] P. Jiao, J. Mueller, J.R. Raney, X.R. Zheng, A.H. Alavi, Mechanical metamaterials and beyond, Nat. Commun. 14 (6004) (2023).
[7] L.R. Meza, A.J. Zelhofer, N. Clarke, A.J. Mateos, D. Kochmann, J.R. Greer, Resilient 3D hierarchical architected metamaterials, Proc. Natl. Acad. Sci. 112 (37) (2015) 11502–11507.
[8] J. Ghoussoub, Y. Tang, W. Dick-Cleland, A. Nemeth, Y. Gong, D. McCartney, A. Cocks, R. Reed, On the influence of alloy composition on the additive manufacturability of ni-based superalloys, Metall. Mater. Trans. A 53 (2022) 962–983.
[9] Y.T. Tang, C. Panwisawas, J.N. Ghoussoub, Y. Gong, J.W.G. Clark, A.A.N. Németh, D.G. McCartney, R.C. Reed, Alloys-by-design: application to new superalloys for additive manufacturing, Acta Mater. 202 (2021) 417–436.
[10] S. Murray, K. Pusch, A. Polonsky, C. Torbet, G. Sweard, N. Zhou, S. Forsik, P. Nandwana, M. Kirka, R. Dehoff, W. Slye, T. Pollock, A defect-resistant Co-Ni superalloy for 3D printing, Nat. Commun. 11 (2020) 4975.
[11] Y.T. Tang, J.N. Ghoussoub, C. Panwisawas, D.M. Collins, S. Amirkhanlou, J.W.G. Clark, A.A.N. Németh, D. Graham McCartney, R.C. Reed, The effect of heat treatment on tensile yielding response of the new superalloy abd-900am for additive manufacturing, in: S. Tin, M. Hardy, J. Clews, J. Cormier, Q. Feng, J. Marcin, C. O'Brien, A. Suzuki (Eds.), Superalloys 2020, Springer International Publishing, Cham, 2020, pp. 1055–1065.
[12] Y.T. Tang, C. Panwisawas, B.M. Jenkins, J. Liu, Z. Shen, E. Salvati, Y. Gong, J.N. Ghoussoub, S. Michalik, B. Roebuck, P.A. Bagot, S. Lozano-Perez, C.R. Grovenor, M.P. Moody, A.M. Korsunsky, D.M. Collins, R.C. Reed, Multi-length-scale study on the heat treatment response to supersaturated nickel-based superalloys: precipitation reactions and incipient recrystallisation, Addit. Manuf. 62 (2023) 103389.
[13] L.J. Gibson, M.F. Ashby, Cellular Solids, Cambridge University Press, 1997.
[14] A. Németh, D. Crudden, D. Armstrong, D. Collins, K. Li, A. Wilkinson, C. Grovenor, R. Reed, Environmentally-assisted grain boundary attack as a mechanism of embrittlement in a nickel-based superalloy, Acta Mater. 126 (2017) 361–371.
[15] Mechanical and physical properties of austenitic chromium-nickel stainless steels at ambient temperatures, Tech. Rep. 2978, Nickel Institute, 1963.
[16] H. Tammpere, P. McKeown, J. Miller, C. Fang, E. Curtis, M. Gaiser-Porter, M. Burley, J. Campbell, M. Artiles, Y. Tang, S. Utada, R. Reed, T. Clyne, Profilometry-based indentation plastometry at high temperature, Adv. Eng. Mater. 26 (21) (2024) 2301073.
[17] S.V. Senkova, O.N. Senkov, D.B. Miracle, Cryogenic and elevated temperature strengths of an al- zn- mg- cu alloy modified with sc and zr, Metall. Mater. Trans. A 37 (2006) 3569–3575.
[18] T. Nawaya, W. Beck, A. von Hehl, Tensile properties of α-titanium alloys at elevated temperatures, in: The 14th World Conference on Titanium, 2020.
[19] Special Metals Corporation, Inconel alloy 718, Tech. Rep. Publication number SMC-045, Special Metals Corporation, 2007.
[20] I. Polmear, D. StJohn, J.-F. Nie, M. Qian, Light Alloys: Metallurgy of the Light Metals, Butterworth-Heinemann, 2017.